

Quantifying native and cut edge recombination of silicon solar cells

W. Wöhler^{a,*}, J.M. Greulich^a, A.W. Bett^{a,b}

^a Fraunhofer Institute for Solar Energy Systems, Heidenhofstraße 2, 79110 Freiburg, Germany

^b Albert-Ludwigs-University, Physical Institute, Hermann-Herder-Straße 3, 79104 Freiburg, Germany

ARTICLE INFO

Keywords:

Silicon solar cells
Edge recombination
Characterization

ABSTRACT

To measure edge recombination of silicon solar cells, a refined perimeter to area methodology is presented and applied to a set of finished silicon heterojunction (SHJ) solar cells from an industrial batch. Different sample sizes are cut from these by thermal laser separation (TLS), giving samples with thermally cleaved, laser scribed and natively processed edges that are investigated. Surface recombination velocities are determined for all three edge types at injection levels of $\Delta n = (10^{14} \text{ to } 10^{15}) \text{ cm}^{-3}$, with values at $\Delta n = 10^{15} \text{ cm}^{-3}$ being $S_{\text{native}} = 250 \text{ cm/s}$, $S_{\text{TLS}} = 750 \text{ cm/s}$ and $S_{\text{scribe}} = 11000 \text{ cm/s}$. The injection dependence is dominated by recombination of ideality 2, with line-specific saturation current densities of $j_{02,\text{native}}^{\lambda} = 2.41 \text{ nA/cm}$, $j_{02,\text{TLS}}^{\lambda} = 7.77 \text{ nA/cm}$ and $j_{02,\text{scribe}}^{\lambda} = 115 \text{ nA/cm}$. The corresponding efficiency losses are approximated by numerical simulations with $\Delta\eta_{\text{native}} = -0.1\%$ for the full cell as well as $\Delta\eta_{\text{TLS,half}} = -0.3\%$ and $\Delta\eta_{\text{TLS,shingle}} = -1.1\%$ for the TLS-cut half- and shingle cells. Overall, the method can be employed to quantify injection-level-dependent edge recombination on finished solar cells for accurate edge loss analysis and process optimization.

1. Introduction

Edge recombination becomes an important factor for solar cells approaching the theoretical limit of silicon solar cells [1,2]. While the edge losses are mitigated by larger wafers, production processes and module integration both place constraints on the sizes of raw wafers and finished cells, respectively. In detail, wafer handling and lateral process homogeneity are challenges of large wafers in production, with edge lengths of 182 mm, 210 mm and variations thereof commonly being used in industry. The resulting native edge may include wrap-arounds of amorphous silicon and TCO layers in silicon heterojunction solar cells or edge inhomogeneities due to single-sided wet chemical processes in TOPCon solar cells. Also, half and shingle cell layouts are typically used, with additional edges induced by the separation process. Overall, native and cut edges are both commonly present in silicon solar cells and accurate characterization can effectively help to analyze and reduce edge recombination. As charge carrier recombination is a fundamental semiconductor property, it is observable with numerous silicon solar cell characterization techniques. Characteristic figures commonly used to quantify recombination are the open-circuit voltage V_{oc} , the implied open-circuit voltage iV_{oc} or the pseudo fill factor pFF . Also, characteristic curves like $I_{\text{sc}}-V_{\text{oc}}$, $S_{\text{uns}}-V_{\text{oc}}$ or quasi-steady-state photoconductance (QSSPC) curves are dominantly shaped by the recombination properties of the solar cell. Furthermore, image data from photoluminescence (PL) and electroluminescence (EL) techniques can

be used to characterize recombination with spatial resolution. While many measurements are sensitive to recombination, it is inherently challenging to distinguish different recombination channels because localized recombination properties, like the edge, are averaged out by the good electrical interconnection within the solar cell. Spatially resolved imaging techniques furthermore suffer from abruptly changing optical properties at the edge, leading to ambiguous interpretations [3]. Over the past three decades, different approaches have been devised to tackle this problem, which we briefly review in the following. Simple diode models have been fitted to dark IV [4,5], $S_{\text{uns}}-V_{\text{oc}}$ [6–9] and other measurements [10,11], as well as an elaborated FEM model to a combination of light IV, $S_{\text{uns}}-V_{\text{oc}}$ and PL-images [12]. By combining this with a perimeter-to-area (P/A)-analysis, characteristic diode saturation currents of ideality 2 with $J_{02,\text{edge}}^{\lambda} = (0.5 \text{ to } 20) \text{ nA/cm}$ have been reported within these works. A few publications also found values exceeding this range for heavily laser-scribed edges [4,12]. FEM model fits to describe PL-gradients also have been used [13] and theoretical simulations further suggest, in accordance with experimental results, an upper limit of roughly $J_{02,\text{max}}^{\lambda} \approx 20 \text{ nA/cm}$ for a bare p–n junction [14,15]. Publications that focus on passivation processes often use qualitative measurements, like the V_{oc} or pFF at low intensities [16–19]. Overall, the methods to characterize edge recombination, which have been used to date, are either qualitative or require explicit model

* Corresponding author.

E-mail addresses: wilkin.woehler@ise.fraunhofer.de (W. Wöhler), johannes.greulich@ise.fraunhofer.de (J.M. Greulich), andreas.bett@ise.fraunhofer.de (A.W. Bett).

<https://doi.org/10.1016/j.solmat.2024.113192>

Received 16 August 2024; Received in revised form 23 September 2024; Accepted 23 September 2024

Available online 8 October 2024

0927-0248/© 2024 The Authors. Published by Elsevier B.V. This is an open access article under the CC BY license (<http://creativecommons.org/licenses/by/4.0/>).

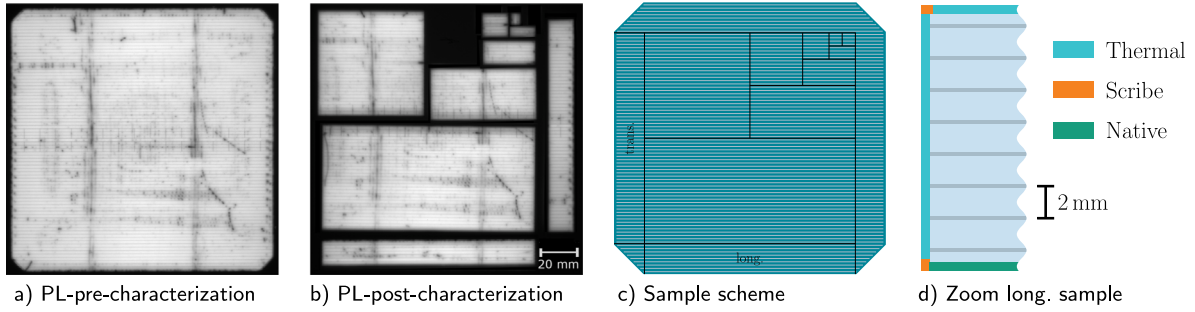


Fig. 1. PL images in arbitrary units of solar cell and sample scheme. (a) Pre-characterization by PL imaging to select homogeneous cells. (b) Post-characterization by PL imaging to detect handling damages that may increase recombination systematically. (c) Cutting scheme optimized to include wide range of P/A ratios and utilize samples efficiently. (d) Edge types indicated exemplarily at left side of long-sample with initial scribe length drawn to scale.

assumptions of the underlying physical properties. Moreover, thermal laser separation (TLS), which is the common solar cell separation process in industry, requires an initial laser scribe that is propagated thermally through the wafer, leading to multiple edge types on each sample, as indicated in Fig. 1(d), which is an other topic that has not been addressed to our knowledge.

In this work, we refine the characterization of edge recombination by proposing a method to extract surface recombination velocities of solar cell edges, independent of the underlying recombination mechanisms, from I_{sc} - V_{oc} measurements. In a first section, we describe our methodology including experimental samples and measurements thereof. In the following calculations, we define a localized model of edge recombination, motivate the sample design and highlight some caveats regarding it. Also, we provide a possible parameterization of the surface recombination velocity in terms of saturation current densities with ideality 1 and 2, to compare our finding to those from literature. Finally, we present the results of the method and discuss its strengths, limitations and applications.

2. Experimental

2.1. Description of samples

Four representative test samples were used from a larger batch of n-type silicon heterojunction (SHJ) solar cells from an industrial mass production. The samples were selected from the batch, by calculating the L2-norm between the IV-parameters (η , V_{oc} , J_{sc} , FF) with their corresponding median, each normalized by the standard deviation of the underlying distribution. The IV-parameters of the selected cells have a very narrow distribution, on the order of the measurement uncertainty. The cells have a rear emitter, a thickness of $d_{cell} = 145 \mu\text{m}$ and a side length of $L_{cell} = 166 \text{ mm}$ (M6). Efficiencies are measured in the range of $\eta = (22.8 \text{ to } 22.9) \%$, with open-circuit voltages between $V_{oc} = (739 \text{ to } 740) \text{ mV}$, fill factors between $FF = (80.7 \text{ to } 80.8) \%$ and short-circuit currents between $J_{sc} = (38.02 \text{ to } 38.05) \text{ mA/cm}^2$. The bulk resistivity is approximately $\rho_{bulk} = 1.2 \Omega\text{cm}$, corresponding to a dopant density of $N_D = 4.1 \times 10^{15} \text{ cm}^{-3}$. Typical minority carrier lifetimes of $\tau_{QSSPC} = 2 \text{ ms}$ were measured at an injection level $\Delta n = 10^{15} \text{ cm}^{-3}$ on reference samples using the quasi-steady-state photoconductance (QSSPC) method.

2.2. Processing of samples

To separate the differently sized samples for the P/A analysis, we use the thermal laser separation (TLS) process of the tool 3D-MicroDICE[®], with a laser wavelength of $\lambda_{laser} = 1070 \text{ nm}$ in pulsed mode for the initial scribe process and continuous wave mode for the thermal cleave process, similar to the processes described in [18,19]. While the actual thermal cleave introduces only little additional damage to the samples, it requires an initial laser scribe of about $500 \mu\text{m}$ length,

as depicted in Fig. 1(d), that is highly recombination-active [20] and which we account for in the analysis. The cutting scheme of the cells is shown in Fig. 1(c). The sample design provides three different types of samples that place different constraints on the model fit.

First, the full cell incorporates the largest core cell area and the native edge, but with a low P/A ratio. Hence, the sample determines the core lifetime well and the surface recombination velocity of the native edge moderately. Second, the sets of differently sized rectangles and squares constitute a straight-forward separation scheme for a P/A analysis, characterizing the core lifetime and the recombination parameters of the two cut edge types (laser-scribed and thermally cleaved) in the experiment. Third, the separated samples of the edge along the fingers and transverse to the fingers, named in Fig. 1(c) “long.” and “trans.”, have a high P/A ratio, with the native edge accounting for roughly 40 % of the total perimeter. As the scribed and cleaved edges are already well constrained by the previous structures, these samples place the strongest constraints on the surface recombination velocity of the native edge. Overall, the sample design constrains all edge types present in our samples and efficiently uses the material and cutting processes. Also, it accommodates for the same number of initial scribes on each sample, to simplify the evaluation. PL imaging is employed before and after each cleaving and measurement step, to identify systematic errors originating from localized recombination-active areas or handling damages. Examples of the pre- and post-characterization are provided in Fig. 1(a) and (b), respectively.

2.3. Measurements and data processing

For the analysis, we utilize I_{sc} - V_{oc} measurements to effectively measure average excess charge carrier lifetimes $\tau_{eff}(\Delta n)$ of the samples at injection levels between $\Delta n = (10^{12} \text{ to } 10^{16}) \text{ cm}^{-3}$, with more details discussed in Section 3.1. These lifetimes are interpolated for the analysis at logarithmically spaced injection levels. To suppress the impact of outliers due to additional damages, we use the maximum lifetime of each sample group and injection level as a representative value. The uncertainty of the representative values is estimated by the standard deviation within each group, if more than one sample is available. For one of the groups, only one sample was valid, for which we conservatively set the relative uncertainty to 50 %. The data at this stage is depicted in Fig. 2, omitting uncertainties for clarity. As expected, we find lower effective lifetimes for smaller samples, which have a higher P/A ratio. Nevertheless, we cannot distinguish the substructure related to the different edge types or to the injection level, yet. The necessary analysis is described in Section 3.4.

3. Calculation and analysis

3.1. Localized edge recombination model

Within solar cells, different domains can be qualitatively distinguished by different recombination mechanisms. However, in actual

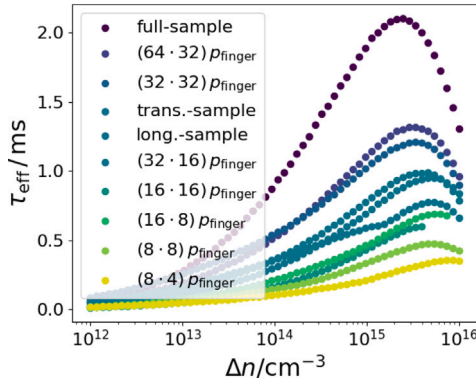


Fig. 2. Overview of representative lifetimes $\tau_{\text{eff}}(\Delta n)$ after data processing, with coloring and label order by P/A ratio. The samples that include the native edge are named by full-, trans.- and long.-sample. In this ordering, they correspond to the cell before separation and the outer samples where fingers are either transversal or longitudinal to the stripe. The naming of the inner rectangles describes the geometrical length and width in terms of the finger pitch of $p_{\text{finger}} = 2074 \mu\text{m}$.

devices only effective electrical quantities are measurable, as the metal grid and conductive layers average out localized properties. To model the impact of localized recombination parameters on the average recombination, we describe the solar cell by a thin cuboid with a large front and rear side area A_{cell} and a thickness d_{cell} . While in true devices the injection level Δn is not perfectly homogeneous over the whole device, we approximate it to be constant over the whole volume, which is mostly justified for solar cells with passivated contacts like SHJ- and TOPCon-concepts. In this sense, the edge-related recombination parameters have to be understood as effective quantities. The average recombination rate density under open-circuit condition r_{oc} is probed over a wide range of injection levels by $I_{\text{sc}}-V_{\text{oc}}$ measurements. From these curves, we calculate the effective lifetime depending on the average injection level $\tau_{\text{eff}}(\Delta n)$ that is defined by

$$r_{\text{oc}}(\Delta n) = \frac{\Delta n}{\tau_{\text{eff}}(\Delta n)}. \quad (1)$$

The conversion of $I_{\text{sc}}-V_{\text{oc}}$ -measurements to effective lifetime curves, follows earlier works from the literature [21,22]. It expresses the injection level in terms of the quasi Fermi level splitting (QFS), which is measured by the open-circuit voltage V_{oc} . The effective lifetime is then calculated from the short-circuit current density J_{sc} , which defines r_{oc} , in conjunction with the determined injection level. For the localized description of recombination, we distinguish all edge types and a homogeneous core cell area as different domains. The lumped recombination rate density is then defined by

$$r_{\text{lumped}} = r_{\text{core}} + \sum_{i \in \text{Edges}} l_i \frac{r_i^{\sigma}}{A_{\text{cell}}} \quad (2)$$

with the surface recombination rate densities r_i^{σ} to describe recombination on the wafer sides for different edge types of length l_i , and the average core recombination rate density r_{core} that includes bulk as well as surface recombination on front and rear side. In a next step, we express the surface recombination rate densities of the different edges, r_i^{σ} , in terms of surface recombination velocities S_i and the average core volume recombination rate density r_{core} in terms of a lifetime τ_{core} .

$$r_i^{\sigma} = S_i \Delta n \quad (3)$$

$$r_{\text{core}} = \Delta n / \tau_{\text{core}} \quad (4)$$

Inserting these relations into Eq. (2) yields

$$r_{\text{lumped}} = \Delta n \left(\frac{1}{\tau_{\text{core}}} + \sum_{i \in \text{Edges}} l_i \frac{S_i}{A_{\text{cell}}} \right). \quad (5)$$

By setting r_{lumped} from Eq. (5) equal to the open-circuit recombination rate density r_{oc} from Eq. (1), we end at the parameterization of the effective cell lifetime in terms of the localized recombination properties.

$$\frac{1}{\tau_{\text{eff}}(\Delta n)} = \frac{1}{\tau_{\text{core}}} + \sum_{i \in \text{Edges}} l_i \frac{S_i}{A_{\text{cell}}} \quad (6)$$

The localized recombination model that we have derived, is very simple and suitable for numerical fits. However, we want to note two limitations due to the assumptions used. First of all, we assumed a homogeneous injection level, which might not be present for highly recombination-active regions or regions in a cell that are poorly electrically connected to the core volume of the cell. Second, we calculated the surface recombination velocities under the assumption of flat edges, which is questionable in the case of the scribed sample, where residual silicon melt from the laser process may form larger surfaces. In this case, the obtained surface recombination velocities are only meaningful in connection with the edge area that is used within the analysis.

3.2. Considerations regarding sample shapes

For samples with a single edge type, we find that the effective recombination rate $r_{\text{eff}} = \tau_{\text{eff}}^{-1}$ scales linearly with the P/A -ratio. In this case, the slope is proportional to the surface recombination velocity of the edge S_{edge} and the y-intercept is proportional to the inverse of the core lifetime τ_{core} . In the more general case of samples with multiple edge types, i.e. TLS samples with partly laser scribed and partly thermally cleaved edges, the analysis becomes more complicated, as the fitting procedure has to account for the varying edge lengths. This is addressed by the parameterization in Eq. (6). However, a caveat has to be considered when dealing with typical TLS-samples, which require an initial laser scribe of fixed length that is highly recombination-active. In such a setup, a design of experiment that consists of stripes of different lengths leads to an ambiguity within the fit parameters of the model. To illustrate the problem, we compare theoretically a stripe sample scheme with a rectangular sample scheme for the TLS-process in the following. For the TLS-processed edges, we assume a fixed initial scribe length l_A on each sample, with a surface recombination velocity S_A . The surface recombination velocity of the remaining thermally cleaved perimeter is denoted by S_B .

The stripes in the first sample scheme are described by a length l_{st} , width $w_{\text{st}} = f_{\text{st}} l_{\text{st}}$ and corresponding area $A_{\text{st}} = f_{\text{st}} l_{\text{st}}^2$, where f_{st} is the aspect ratio that is varied as the independent variable in the experiment. Inserting these geometrical relations into Eq. (6) yields

$$\frac{1}{\tau_{\text{eff, st}}} = \frac{1}{\tau_{\text{core}}} + \frac{l_A S_A}{f_{\text{st}} l_{\text{st}}^2} + \frac{2l_{\text{st}}(1 + f_{\text{st}}) - l_A}{f_{\text{st}} l_{\text{st}}^2} S_B \quad (7)$$

$$= \left(\frac{1}{\tau_{\text{core}}} + \frac{2S_B}{l_{\text{st}}} \right) + \frac{1}{f_{\text{st}}} \frac{l_A S_A + (2l_{\text{st}} - l_A) S_B}{l_{\text{st}}}. \quad (8)$$

For the rectangular design of experiment, we assume a fixed aspect ratio f_{rec} , a base length l_0 and a scaling factor a , and hence, rectangles of length $l_{\text{rec}} = a l_0$, width $w_{\text{rec}} = a f_{\text{rec}} l_0$ and corresponding area $A_{\text{rec}} = a^2 f_{\text{rec}} l_0^2$. Here, the aspect ratio f_{rec} is fixed and the scaling factor a is the independent variable of the experiment. Inserting the rectangular geometrical relations into Eq. (6) yields

$$\frac{1}{\tau_{\text{eff, rec}}} = \frac{1}{\tau_{\text{core}}} + \frac{l_A S_A}{a^2 f_{\text{rec}} l_0^2} + \frac{2(a l_0 + a f_{\text{rec}} l_0) - l_A}{a^2 f_{\text{rec}} l_0^2} S_B \quad (9)$$

$$= \frac{1}{\tau_{\text{core}}} + \frac{1}{a} \frac{2(1 + f_{\text{rec}}) S_B}{f_{\text{rec}} l_0} + \frac{1}{a^2} \frac{l_A (S_A - S_B)}{f_{\text{rec}} l_0^2}. \quad (10)$$

To fit all three parameters S_A , S_B and τ_{core} , three linearly independent responses of the effective lifetime are required. While the stripe design of experiment only exhibits a constant and linear dependence on the inverse aspect ratio f_{st} , we find a constant, linear and quadratic dependence on the corresponding inverse scaling factor a in the case of a rectangular design of experiment for $S_A \neq S_B$. Hence, when

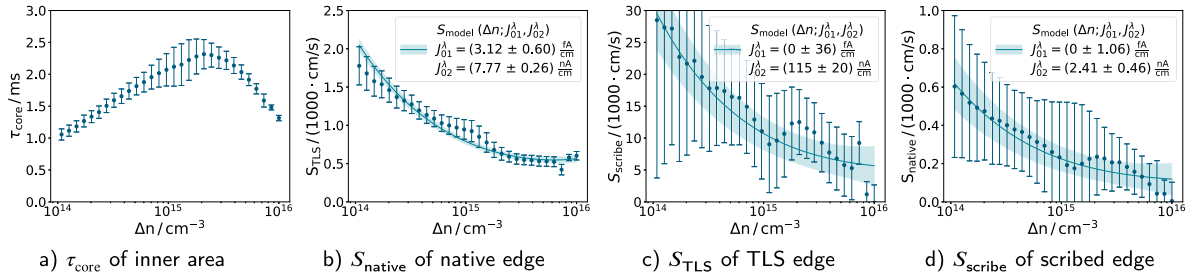


Fig. 3. In (a) to (d), the scattered points depict the optimal parameters of the localized recombination model, which best describe the effective lifetime measurements at each injection level separately. A parameterization of the surface recombination velocity by J_{01} - and J_{02} -recombination is also fitted to the results and depicted by the lines with the shading corresponding to the parameter uncertainties.

using a stripe design to determine the recombination parameters of the TLS-process, additional sample variations are required to constrain the numerical fits sufficiently. In a nutshell, we can draw the conclusion that a rectangular sample design circumvents some ambiguities in the description of the effective lifetime by localized recombination parameters, and is expected from this analysis to yield more stable fit results.

3.3. Parameterization of SRV

The model that we derived in Section 3.1 can be evaluated at every injection level separately, with the series of optimal fit parameters describing the injection-level dependence of the recombination parameters. In comparison, previous publications in the literature commonly assumed characteristic saturation current densities with different ideality factors to evaluate the edge recombination [4–12]. To draw the comparison of our results to these literature values, we parameterize the surface recombination velocity in terms of saturation current densities, and fit this recombination model to our data. To this purpose, we may write the recombination rate density r_S^σ due to a surface recombination velocity $S(\Delta n)$ at a given excess carrier density Δn as

$$r_S^\sigma(\Delta n) = S(\Delta n)\Delta n. \quad (11)$$

Moreover, we can express the corresponding area-related recombination rate density r_{j0m}^σ with j_{0m} -characteristic by the Shockley diode equation and reformulate the exponential part in terms of the carrier densities.

$$r_{j0m}^\sigma(\Delta n) = j_{0m}^\lambda \frac{d_{\text{cell}}}{e} \exp\left(\frac{V(\Delta n)}{mV_t}\right) \quad (12)$$

$$= j_{0m}^\lambda \frac{d_{\text{cell}}}{e} \left(\frac{(\Delta n + N_b)\Delta n}{n_i^2}\right)^{\frac{1}{m}} \quad (13)$$

Here, j_{0m}^λ denotes the line-specific diode saturation current density, m the ideality factor, e the elementary charge, d_{cell} the cell thickness, $V(\Delta n)$ the voltage across the junction and $V_t = e/(k_B T)$ the thermal voltage, with the Boltzmann constant k_B and temperature T . We assume a sum of j_{01}^λ and j_{02}^λ recombination for the device at hand, which is common to describe surface recombination in the literature. Setting the sum ($r_{j01}^\sigma + r_{j02}^\sigma$) equal to the recombination rate density r_S^σ from Eq. (11), we find

$$S_{\text{model}}(\Delta n) = \frac{d_{\text{cell}}}{e} \left[j_{01}^\lambda \left(\frac{\Delta n + N_b}{n_i^2}\right) + j_{02}^\lambda \sqrt{\frac{\Delta n + N_b}{n_i^2 \Delta n}} \right]. \quad (14)$$

3.4. Perimeter to area analysis

To extract the recombination parameters of the different edges, we conduct a P/A -analysis at each injection level independently, by fitting the localized recombination model that is discussed in Section 3.1 to the set of representative lifetimes, originating from all sample types.

The model is thereby defined in terms of physically interpretable parameters such that the optimal parameters with statistical uncertainties of the fit correspond directly to the lifetime of the core cell, as well as the surface recombination velocities of the edges. As we conduct each P/A -analysis independently at each injection level, a continuous injection-level dependence of the optimal parameters is a validation of a stable fitting procedure. While the result could in principle be used as a direct input for physical device simulations, we further describe the injection-level dependence of the obtained surface recombination velocities, by a sum of characteristic J_{01} - and J_{02} -recombination as described in Section 3.2. The fit of the injection-level dependence yields the optimal dark saturation current densities, which can be compared to previous findings from the literature, or used to parameterize the edge recombination in simulations.

4. Results and discussion

4.1. Fit quality and uncertainty

The optimal parameters of the fit are shown in Fig. 3. Well visible is that the optimal parameters of the independent least square fits form continuous curves, indicating stable convergence of the fits over the whole interval under investigation. The varying uncertainties of the curves for different edge types, are mostly related to the corresponding total edge length that is included within the dataset and analysis. Therefore, it would be possible to reduce the uncertainty of one of the fitted recombination parameters by adding dedicated samples with a larger ratio of the corresponding edge to the analysis. This is easily conceivable for the scribed edge, see Fig. 1(d), however for the native edge more cells would be required, as each cell has a fixed native edge length. We speculate that using a larger sample number would also reduce the bumps within the curve progressions, which are related to different samples dominating the representative average lifetime of a sample group at different injection levels. Overall, the analysis based on only four full sized solar cells already yields stable results for the edge recombination parameters over a wide range of injection levels.

4.2. Fit results and comparison to literature

Within the analysis, a size-independent core lifetime is obtained that is comparable to the initially measured minority charge carrier lifetime of the full cell, $\tau_{\text{QSSPC}} \approx 2 \text{ ms}$ at an injection level of $\Delta n = 10^{15} \text{ cm}^{-3}$. The proposed method further yields the injection-level dependence of the core lifetime as well as of the edge surface recombination velocities. Within the studied interval of the injection level, $\Delta n = (10^{14} \text{ to } 10^{16}) \text{ cm}^{-3}$, all three edge surface recombination velocity curves show a similar injection-level dependence on first sight. Comparing the maximal values of the curves, we find a clear ordering between the three different edge types. As expected from works utilizing V_{OC} , FF or pFF of separated solar cells, the passivated native cell edge shows the smallest surface recombination velocity with a maximum of

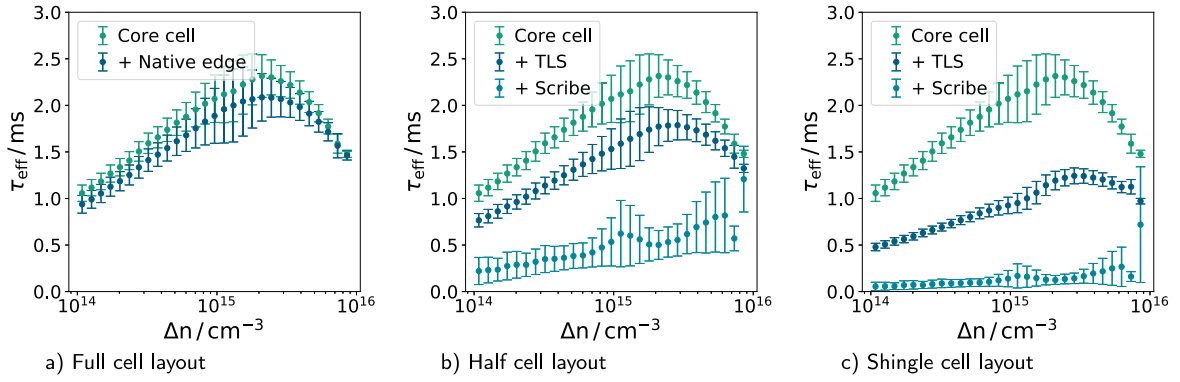


Fig. 4. Application of edge characterization results and model to illustrate the reduced lifetime due to edge recombination in different cell layouts. All diagrams include the core cell lifetime as reference value that excludes all edge recombination. (a) full M6 solar cell with native edges. (b) M6 half cell design, with one long side cut either by the TLS or Scribe process. (c) M6, 5-shingle design, with two long sides cut either by the TLS or Scribe process.

$S_{\text{native, max}} = 600 \text{ cm/s}$. Next, the thermally cleaved edge is expected to exhibit a bare pn-junction and silicon interface, only covered by a thin oxide. In accordance, it shows a roughly three times larger surface recombination velocity than the passivated edge of $S_{\text{TLS, max}} = 1700 \text{ cm/s}$. Finally, the scribed segments exhibit distinctively higher values of $S_{\text{scribe, max}} = 27000 \text{ cm/s}$, as expected for the cruder separation process. While the general ordering of edge quality has been observed before in various works [17–20], the analysis proposed here further quantifies the edge recombination for a typical TLS-process explicitly.

The results obtained here are also coherent in the context of general studies regarding surface recombination velocities at silicon interfaces. There, typical values for passivated surfaces of $S_{\text{pass}} = (10^1 \text{ to } 10^3) \text{ cm/s}$ and for unpassivated surfaces of $S_{\text{bare}} = (10^4 \text{ to } 10^6) \text{ cm/s}$ have been reported under different conditions [23–26].

4.3. Comparison to J_{02}^{λ} from literature

To compare our results with previous values from the literature, we parameterize the surface recombination velocity in terms of characteristic J_{01} and J_{02} recombination, as proposed in Eq. (14), and fit it to the results. Thereby, we do not include bulk recombination mechanisms, like Auger or SRH recombination, as we expect the values of the fitted parameters to originate solely from surface recombination. The injection-level-dependent model fits are well compatible within their uncertainties with the measured surface recombination velocities, as is visible in Fig. 3. Systematic uncertainties due to the used fit range have been found to be accurately quantified by the provided fit uncertainties. In line with literature findings, the edge recombination is dominated by diode recombination of ideality 2, with significant contributions of ideality 1 only present in the thermally cleaved edge segments, probably due to the bare silicon surfaces. The fitted value of the line-specific diode saturation current density J_{02}^{λ} of the native edge is given by $J_{02, \text{native}}^{\lambda} = (2.41 \pm 0.46) \text{ nA/cm}$, and the one of the thermally cleaved edge by $J_{02, \text{TLS}}^{\lambda} = (7.77 \pm 0.26) \text{ nA/cm}$. While these two results fall into the range between $J_{02, \text{lit}}^{\lambda} = (0.5 \text{ to } 20) \text{ nA/cm}$ that is commonly reported in the literature, the value of the scribed edge, $J_{02, \text{scribe}}^{\lambda} = (115 \pm 20) \text{ nA/cm}$, exceeds the often assumed theoretical upper bound of $J_{02, \text{max}}^{\lambda} = 20 \text{ nA/cm}$ for a bare edge of a pn-junction [14,15]. Nevertheless, some publications have also reported values of J_{02}^{λ} exceeding this limit for heavily scribed samples [4,12]. Hence, we speculate that this finding merely indicates severe damage at the scribed edge, possibly due to residual melt increasing the effective edge area or length of the bare pn-junction.

4.4. Implications for different cell layouts

While the proposed description of localized recombination in Eq. (6) allows for a P/A -analysis of samples including multiple edge types, it

can also be applied vice versa to estimate effective lifetimes of new samples. In Fig. 3, we depict the impact of the characterized edge recombination on the effective lifetime for common solar cell layouts, including a full cell, a half cell and a fifth shingle cell, with side lengths of $L_{\text{cell}} = 166 \text{ mm}$ (M6). The full cell is modeled as a pseudo-square area with a diagonal length of $L_{\text{diagonal}} = 223 \text{ mm}$ and a perimeter recombination that corresponds to the native edge. The half cell layout and shingle cell layout are both modeled as rectangular areas with either one or two long edges exhibiting the recombination characteristic of a cut edge, while the remaining perimeter is modeled by the recombination characteristic of the native edge. For the separated cell layouts, we consider both, the TLS- and the scribe-cutting process, to highlight the importance of the edge quality. To compare the different setups, we use the relative lifetime reduction under operational cell conditions, for which we choose $\Delta n = 10^{15} \text{ cm}^{-3}$. In the case of the full cell, the additional edge recombination reduces the lifetime by less than 10 %, leading to moderate losses in the power conversion efficiency. The lifetime of the half cell layout using TLS is already reduced by 25 % and the one using the scribe-process by 73 %, where especially the latter, leads to a severe loss in efficiency. However, the impact is most drastic for the shingle layout, where the thermally cleaved edge leads to a lifetime reduction of 55 % and the scribe-cut edge to a reduction of 93 %. In order to compare the lifetime reductions with values from the literature, we estimate the efficiency losses due to the additional edge recombination in a typical SHJ solar cell, using the simulation software Quokka3 [27]. In Fig. 4, an absolute efficiency loss of $\Delta\eta_{\text{native}} = -0.1 \%$ is observed for the native edge (a), $\Delta\eta_{\text{half, TLS}} = -0.3 \%$ for the TLS cut half cell (b), and $\Delta\eta_{\text{shingle, TLS}} = -1.1 \%$ for the TLS cut shingle cell (c). The scribe process introduces very large efficiency losses of $\Delta\eta_{\text{half, scribe}} = -1.1 \%$ for the half cell and $\Delta\eta_{\text{shingle, scribe}} = -5.5 \%$ in the case of the shingle cell. The findings are consistent with experimental values [18,19,28,29] as well as other simulated values [15,30,31] from the literature. The results emphasize the importance of high edge quality for shingle solar cell layouts, requiring optimized TLS-processes and/or edge passivation schemes. Also, it provides an incentive to cut wafers before processing, which is actually done in new solar cell factories for half cells.

5. Summary and conclusion

Within this work, we first highlight the importance of accurate edge characterization and revisit earlier methods from the literature. The quantitative ones thereby employ a variety of effective diode models that are fitted to IV -curves, in combination with P/A -analysis to obtain line-specific dark saturation current densities. Similar to previous works, the here proposed method utilizes $I_{\text{sc}}\text{-}V_{\text{oc}}$ measurements to efficiently probe recombination of samples in a wide range of injection levels. In contrast to other approaches, it evaluates the

edge recombination by means of an elaborated P/A -analysis at each injection level separately, and hence, is not constrained to a specific recombination model. The method is tested on a set of four industrial M6 SHJ-solar cells, which are cut into samples of different size, employing the TLS-process that requires an initial laser scribe. The analysis yields the surface recombination velocities of the different edge types and the average lifetime of the homogeneous core cell area at injection levels covering $\Delta n = (10^{14} \text{ to } 10^{16}) \text{ cm}^{-3}$. Evaluated under operational conditions, for which we assume $\Delta n = 10^{15} \text{ cm}^{-3}$, we find an average core cell lifetime of $\tau_{\text{core}} = 2 \text{ ms}$ and edge recombination velocities of $S_{\text{native}} = 250 \text{ cm/s}$ for the native edge, $S_{\text{TLS}} = 750 \text{ cm/s}$ for the thermally cleaved edge and $S_{\text{Scribe}} = 11\,000 \text{ cm/s}$ for the laser-scribed edge. To compare these results to those from the literature, we fit the injection dependence of the edge surface recombination velocities by a sum of characteristic J_{01}^{λ} and J_{02}^{λ} recombination. In accordance with other studies, we find that the edge recombination is dominated by a J_{02} -contribution. For the different edge types, we find $J_{02, \text{native}}^{\lambda} = (2.41 \pm 0.46) \text{ nA/cm}$, $J_{02, \text{TLS}}^{\lambda} = (7.77 \pm 0.26) \text{ nA/cm}$ and $J_{02, \text{Scribe}}^{\lambda} = (115 \pm 20) \text{ nA/cm}$, clearly indicating the different levels of damage introduced by the cutting processes. To investigate the impact of the edges on the effective lifetime, we employ the localized recombination description from Eq. (6), and evaluate the lifetime reduction at operational conditions of $\Delta n = 10^{15} \text{ cm}^{-3}$ for different cell layouts. We find that the native edge of the full cell leads to a relative lifetime reduction of only 10 %, while the TLS-edge of a half cell and a shingle cell imply relative lifetime reductions of about 25 % and 55 %, respectively. These lifetime reductions imply efficiency losses of $\Delta\eta_{\text{native}} = -0.1 \%$ for the native edge, $\Delta\eta_{\text{half, TLS}} = -0.3 \%$ for the half cell and $\Delta\eta_{\text{shingle, TLS}} = -1.1 \%$ for the shingle cell.

Overall, we have proposed a versatile method to quantify edge surface recombination velocities, without assuming an explicit injection dependence. The method can be applied to finished solar cells for accurate analysis of edge recombination losses in various context like edge passivation or cell processing.

CRedit authorship contribution statement

W. Wöhler: Writing – original draft, Visualization, Validation, Methodology, Investigation, Formal analysis, Data curation, Conceptualization. **J.M. Greulich:** Writing – review & editing, Validation, Supervision, Project administration, Investigation, Funding acquisition. **A.W. Bett:** Writing – review & editing, Supervision, Resources.

Declaration of competing interest

The authors declare that they have no known competing financial interests or personal relationships that could have appeared to influence the work reported in this paper.

Data availability

Data will be made available on request.

Acknowledgments

We want to thank Andreas Brand for the fruitful discussion of the sample design, as well as Homeira Hashemi for optimizing the cutting sequence during laser processing. This work was supported by the German Federal Ministry for Economic Affairs and Climate Action within the projects “SALSA” (03EE1096 A) and “KISS-PV” (03EE1129 A).

References

- [1] M.A. Green, E.D. Dunlop, M. Yoshita, N. Kopidakis, K. Bothe, G. Siefer, X. Hao, Solar cell efficiency tables (Version 63), Prog. Photovolt., Res. Appl. 32 (1) (2024) 3–13.
- [2] M.J. Kerr, A. Cuevas, P. Campbell, Limiting efficiency of crystalline silicon solar cells due to Coulomb-enhanced Auger recombination, Prog. Photovolt., Res. Appl. 11 (2) (2003) 97–104.
- [3] M. Bokalić, M. Kikelj, K. Brecl, M. Jankovec, F. Buchholz, V. Mihailitchi, M. Topic, EL and LBIC characterization of cut edge recombination in IBC solar cells, in: 37th European Photovoltaic Solar Energy Conference and Exhibition, 2020, pp. 308–311.
- [4] K. McIntosh, C. Honsberg, The influence of edge recombination on a solar cell's IV curve, in: 6th European Photovoltaic Solar Energy Conference, 2000.
- [5] C. Chan, M. Abbott, B. Hallam, M. Juhl, D. Lin, Z. Li, Y. Li, J. Rodriguez, S. Wenham, Edge isolation of solar cells using laser doping, Sol. Energy Mater. Sol. Cells 132 (2015) 535–543.
- [6] S. Glunz, J. Dicker, M. Esterle, M. Hermle, J. Isenberg, F.J. Kamerewerd, J. Knobloch, D. Kray, A. Leimenstoll, F. Lutz, D. Osswald, R. Preu, S. Rein, E. Schaffer, C. Schetter, H. Schmidhuber, H. Schmidt, M. Steuder, C. Vorgrimmler, G. Willeke, High-efficiency silicon solar cells for low-illumination applications, in: Conference Record of the Twenty-Ninth IEEE Photovoltaic Specialists Conference, 2002, pp. 450–453.
- [7] D. Bertrand, S. Manuel, M. Pirot, A. Kaminski-Cachopo, Y. Veschetti, Modeling of edge losses in Al-BSF silicon solar cells, IEEE J. Photovolt. 7 (1) (2017) 78–84.
- [8] M. Wiesenfarth, M. Steiner, H. Helmers, A.W. Bett, Voltage losses due to the perimeter and dark area in micro-concentrator solar cells, Sol. Energy Mater. Sol. Cells 219 (2021) 110791.
- [9] J. Dicker, Analyse und Simulation von hocheffizienten Silizium-Solarzellenstrukturen für industrielle Fertigungstechniken (Dissertation), Albert-Ludwigs-University Freiburg, 2003.
- [10] F.W. Chen, J.E. Cotter, Contactless technique to quantify the edge-junction recombination in solar cells, Appl. Phys. Lett. 89 (26) (2006) 263509.
- [11] K. Rühle, M.K. Juhl, M.D. Abbott, L.M. Reindl, M. Kasemann, Impact of edge recombination in small-area solar cells with emitter windows, IEEE J. Photovolt. 5 (4) (2015) 1067–1073.
- [12] J. Wong, R. Sridharan, V. Shanmugam, Quantifying edge and peripheral recombination losses in industrial silicon solar cells, IEEE Trans. Electron Devices 62 (11) (2015) 3750–3755.
- [13] H. Stolzenburg, A. Fell, F. Schindler, W. Kwapił, A. Richter, P. Baliozian, M. Schubert, Edge recombination analysis of silicon solar cells using photoluminescence measurements, AIP Conf. Proc. 2147 (2019) 020017.
- [14] R. Kuhn, P. Fath, E. Bucher, Effects of pn-junctions bordering on surfaces investigated by means of 2D-modeling, in: Conference Record of the Twenty-Eighth IEEE Photovoltaic Specialists Conference, 2000, pp. 116–119.
- [15] A. Fell, J. Schön, M. Müller, N. Wöhle, M.C. Schubert, S.W. Glunz, Modeling edge recombination in silicon solar cells, IEEE J. Photovolt. 8 (2) (2018) 428–434.
- [16] P. Albert, A. Jaouad, G. Hamon, M. Volatier, C.E. Valdivia, Y. Deshayes, K. Hinzer, L. Béchou, V. Aimez, M. Darnon, Miniaturization of InGaP/InGaAs/Ge solar cells for micro-concentrator photovoltaics, Prog. Photovolt., Res. Appl. 29 (9) (2021) 990–999.
- [17] P. Baliozian, M. Al-Akash, E. Lohmüller, A. Richter, T. Fellmeth, A. Münzer, N. Wöhle, P. Saint-Cast, H. Stolzenburg, A. Spribille, R. Preu, Postmetallization Passivated Edge Technology for separated silicon solar cells, IEEE J. Photovolt. 10 (2) (2020) 390–397.
- [18] A. Münzer, P. Baliozian, K. Ahmed, A. Nair, E. Lohmüller, T. Fellmeth, A. Spribille, R. Preu, Laser-assisted separation processes for bifacial pSPEER shingle solar cells, in: 37th European Photovoltaic Solar Energy Conference and Exhibition, 2020, pp. 394–399.
- [19] P. Baliozian, A. Münzer, E. Lohmüller, A. Nair, T. Fellmeth, N. Wöhle, H. Höfler, A. Spribille, R. Preu, Thermal laser separation of PERC and SHJ solar cells, IEEE J. Photovolt. 11 (2) (2021) 259–267.
- [20] P. Baliozian, Development and Characterization of Bifacial P-Type Silicon Shingle Solar Cells with Edge Passivation (Dissertation), Albert-Ludwigs-University Freiburg, 2021.
- [21] R.A. Sinton, A. Cuevas, A quasi-steady-state open-circuit voltage method for solar cell characterization, in: 16th European Photovoltaic Solar Energy Conference, Vol. 25, 2000, pp. 1152–1155.
- [22] A. Kimmerle, Diffused Surfaces for Crystalline Silicon Solar Cells - Process Development, Characterization, and Modeling (Dissertation), Albert-Ludwigs-University Freiburg, 2015.
- [23] T. Saitoh, Y. Nishimoto, T. Sawada, H. Hasegawa, A novel contactless and nondestructive measurement method of surface recombination velocity on silicon surfaces by photoluminescence, Japan. J. Appl. Phys. 32 (1S) (1993) 272.
- [24] H. Mackel, A. Cuevas, Determination of the surface recombination velocity of unpassivated silicon from spectral photoconductance measurements, in: Proceedings of 3rd World Conference on Photovoltaic Energy Conversion, Vol. 1, 2003, pp. 71–74.

- [25] D. Baek, S. Rouvimov, B. Kim, T.C. Jo, D.K. Schroder, Surface recombination velocity of silicon wafers by photoluminescence, *Appl. Phys. Lett.* 86 (11) (2005) 112110.
- [26] Y. Ichikawa, R. Ishikawa, M. Konagai, Numerical simulation of edge effects in silicon hetero-junction solar cells, *AIP Adv.* 12 (6) (2022) 065006.
- [27] A. Fell, A free and fast three-dimensional/two-dimensional solar cell simulator featuring conductive boundary and quasi-neutrality approximations, *IEEE Trans. Electron Devices* 60 (2) (2013) 733–738.
- [28] B. Martel, M. Albaric, S. Harrison, F. Dhainaut, T. Desrues, Addressing separation and edge passivation challenges for high efficiency shingle heterojunction solar cells, *Sol. Energy Mater. Sol. Cells* 250 (2023) 112095.
- [29] C. Leon, D. Barakel, V. Burlac, L. Roux, R.B. Abbes, T. Regrettier, O. Palais, F. Torregrosa, Ion implantation investigation for the passivation of cut edge solar cells, *AIP Conf. Proc.* 2826 (1) (2023) 030006.
- [30] V. Giglia, J. Veirman, R. Varache, B. Portaluppi, S. Harrison, E. Fourmond, Influence of edge recombinations on the performance of half-, shingled-and full silicon heterojunction solar cells, in: 37th European PV Solar Energy Conference and Exhibition, 2020, pp. 282–285.
- [31] V. Giglia, R. Varache, J. Veirman, E. Fourmond, Influence of cell edges on the performance of silicon heterojunction solar cells, *Sol. Energy Mater. Sol. Cells* 238 (2022) 111605.